Size-controlled synthesis of phase separated protein condensates with interfacial protein cages

Hyeok Jin Oh,† Yongsuk Lee,† Haerang Hwang, Kibeom Hong, Hyeongjoo Choi, Jin Young Kang, and Yongwon Jung*

Department of Chemistry, Korea Advanced Institute of Science and Technology, Daejeon 34141, Korea.

E-mail: ywjung@kaist.ac.kr

†H.J.O. and Y.L. contributed equally to this work.

Abstract

Phase separation of specific proteins into liquidic condensates is a key mechanism to form membrane-less organelles, which organize diverse cellular processes in space and time. These protein condensates hold immense potential as biomaterials that can contain specific sets of biomolecules with extremely high densities and dynamic liquid properties. Despite their appeal, methods to manipulate protein condensate materials remain largely unexplored. Here, we developed a one-pot assembly method to synthesize coalescence-free protein condensates from a few μm to 100 nm sizes with surface-stabilizing protein cages. We discovered that large protein cages (~30 nm), with precisely tuned interaction strengths to condensates, could effectively localize on condensate surfaces and block coalescence during phase separation. This approach proved applicable to diverse condensates with varying compositions and fluidities. Condensate sizes were concisely controlled by modulating condensate/cage ratios. In addition, we successfully visualized the 3D structures of intact protein condensates with interfacial cages with cryo-electron tomography (ET). Protein cages formed monolayer shells on protein condensates, where cages were slightly buried in condensates with contact angles lower than 90 degree. These cage-covered protein condensates maintained dynamic properties, including the capacity for selective material exchange or recruitment from the external environment.

Introduction

Liquid-liquid phase separation (LLPS) of specific proteins into highly dense liquid droplets has emerged as a key mechanism for the formation of membrane-less organelles (MLOs), which play a

crucial role in temporally and spatially coordinating diverse biochemical processes within cells.[1-3] Protein LLPS is driven by weak, multivalent interactions, leading to the spontaneous clustering of proteins into condensed assembly structures.[4] These protein condensates exhibit dynamic liquid properties, including the ability to exchange with the surrounding environment, undergo fusion events, recruit specific biomolecules, and disassemble as needed.[5] This dynamic behavior allows protein condensates to serve as specialized micro-compartmental hubs, enriched with specific biomolecules, to dynamically regulate cellular activities.[6]

Beyond their essential functions in cells, protein condensates are compelling candidates for biomaterials distinguished by unique features.[7] A specific set of biomolecules can be reversibly packed within confined spaces at unprecedented densities under physiological conditions. The liquid nature provides a dynamic platform with the potential to allow and control communications with outside materials. Additionally, through the manipulation of protein composition or adjustment of environmental conditions, researchers can engineer protein condensates with tailored characteristics.[8] Moreover, serving as intrinsic MLOs, protein condensates can act as ideal compartmental reactors for diverse biomolecular processes. Several recent studies have showcased the versatility of these protein condensate materials, demonstrating their utility as core backbones for artificial cells,[9,10] delivery vesicles for drugs,[11,12] and reactors for biochemical reactions.[13,14]

While protein condensate materials hold significant promise, the synthesis of stable protein condensates with defined size and enduring structural integrity remains a largely unexplored challenge. The formation of protein condensates through LLPS involves continuous nucleation, growth, and fusion (coalescence) processes, leading to intrinsic size fluctuations.[4,15,16] In particular, the continuous coalescence of multiple protein condensates into larger condensates presents a significant obstacle to achieving reliable protein condensate synthesis. Additionally, the fluidic architecture and rather sticky surfaces (with high protein content) of protein condensates make it challenging to maintain condensate structures during various synthesis steps. Complicating matters further, the diverse physical properties and LLPS propensities exhibited by different types of condensates hinder the development of universally applicable synthesis strategies.

Employing a physical barrier on the surface has proven to be the most effective strategy in stabilizing inherently unstable colloidal structures.[17] Amphiphilic surfactants, commonly employed in the synthesis of colloidal micro/nano materials, have been instrumental in mediating interactions between two immiscible components, such as nanoparticles and solvents or water and oil.[18,19] However, the less clear immiscibility between aqueous solutions and protein condensates poses a unique challenge in

designing effective surface-stabilizing agents. A recent study reported the successful engineering of an amphiphilic protein surfactant that hindered the coalescence of protein condensates.[20,21] Still, robust surface-stabilizing methods are required to effectively interrupt protein condensate formation processes and produce condensates with a wide and defined range of sizes.

Beyond amphiphilic surfactants, symmetric small particles offer an alternative for stabilizing colloidal structures, particularly liquidic emulsions, by adsorbing onto the unstable emulsion interface.[22] The stability of these so-called Pickering emulsions can be tuned by adjusting the size and surface binding affinity of the stabilizing particles, referred to as Pickering agents.[23-25] The concept of Pickering emulsions, which does not necessitate amphiphilicity, holds great promise for the stable synthesis of liquidic protein condensates. Indeed, recent studies have reported that certain protein clusters and RNA exhibit Pickering agent-like features, binding to condensate surfaces and impeding condensate coalescence in cells.[26,27] Here, we report a generally applicable method to synthesize stable, coalescence-prevented protein condensates with sizes ranging from a few micrometers down to 100 nanometers by employing interfacial protein cages. Multiple protein cages were engineered as surface stabilizers, and their interactions with condensate surfaces were precisely tuned to produce diverse types of cage-stabilized protein condensates. Precise control over condensate sizes was achieved by adjusting the relative quantities of condensate-forming proteins and interfacial cages, while the resulting condensates retained all dynamic liquid properties. Unique structural features of condensates with surface protein cages were visualized using cryo-ET.

Results and discussions

Synthesis of protein cage-stabilized protein condensates

According to Pickering emulsion theory, the energy required to displace a Pickering particle agent from the emulsion interface depends on the particle's radius and its relative affinities toward both phases, such as oil and water.[28,29] Larger particles, possessing a greater contacting area and adsorption energy, contribute to enhanced surface stabilization. Likewise, maximum energy stabilization occurs when Pickering agents show similar affinities towards both phases. In contrast to emulsions formed with two chemically distinct phases (e.g., oil and water), protein condensates consist of two aqueous phases differing only in protein concentration. We envisioned that the surface stabilization of protein condensates will be primarily influenced by the interaction of interfacial agents with condensate-forming proteins, particularly on the dense condensate phase (Fig. 1a). To develop ideal Pickering agent-like surface stabilizers for protein condensates, we explored protein cages with diverse sizes

ranging from 10-40 nm. Protein cages offer highly uniform sizes, and, more importantly, their interactions with protein condensates can be thoroughly tuned by precise cage engineering.

Protein condensates were prepared using a previously developed metal ion-induced LLPS.[30] Phase-separable proteins, tagged with six His residues (6His), can be clustered by Ni^{2+}, where a Ni^{2+} ion is coordinated by two (or more) 6His tags,[31] leading to subsequent phase separation. Various protein condensates with different properties, such as rigidity, can be formed by switching phase-separable proteins.[30] Moreover, 6His can also be fused to protein cages to mediate interactions between cages and condensates through Ni^{2+}-6His coordination. The strength of this interaction can be further varied by Ni^{2+} concentrations. Initially, rigid and positively charged protein condensates were prepared using a proline-rich motif (PRM) and its binding domain SH3 (PRM-SH3-6His, PSH) (Fig. 1b).[30] PSH condensate droplets were formed by simply mixing PSH and Ni^{2+}. For interfacial protein cages, three cages with different sizes and oligomeric states were engineered: octameric isoaspartyl dipeptidase (POK, ~10 nm)[32], 24-meric human ferritin (HF, ~15 nm)[33], and 60-meric artificial cage mi3 (~25 nm)[34] (Fig. 1c and Fig. S1). Negatively charged GFP was uniformly introduced on all protein cage surfaces to induce cage's electrostatic binding to positive PSH condensates with similar charge densities but with different sizes. Protein cages were prepared also with and without 6His. Additionally, to further increase cage particle size, we assembled multiple ferritins into a spherical structure (HF oligo, ~40 nm), as previously reported.[35] In HF oligo, a single GFP-fused HF is surrounded by 4 – 5 HF cages, and only the core GFP-fused HF is modified with 6His (Fig. S1).

We first examined interactions between protein cages and pre-formed PSH condensates. Protein cages were introduced to PSH condensates 2 min after LLPS induction (final [cage] = 50 μg/mL, [PSH] = 500 μg/mL), and both dye-labelled condensates (Cy5, magenta) and GFP-fused cages (green) were imaged after 10 and 60 minutes of incubation (Fig. 1d). In the absence of protein cages, the size of PSH condensate droplets increased over time, up to 5 μm, likely through condensate coalescence. All (negatively charged) protein cages, as well as control monomeric GFP, strongly adsorbed on (positively charged) PSH condensate surfaces, with the presence of 6His on cages further enhancing this adsorption. The highly dense and rigid structure of PSH condensates might impede further penetration of cages.[30] Despite robust surface binding, HF and POK cages could not prevent condensate coalescence, resulting in condensate growth similar to that observed in free condensates. Interestingly, however, with larger HF oligo and mi3 cages, condensate sizes and morphologies are nearly identical both at 10 min and 60 min, indicating potent surface stabilization and inhibition of coalescence. These findings show the promising potential of properly engineered protein cages as effective stabilizers for protein condensates.

While generated PSH condensates could be effectively stabilized by proper protein cage adsorption, controlling condensate size remained a challenging task. To regulate condensate size, rapidly growing and easily fusing condensates must be trapped and stabilized through cage adsorption. However, the growing kinetics of protein condensates remain largely unexplored, and trapping condensates at the early LLPS stage, especially for smaller condensate synthesis, presents huge practical challenges. Therefore, we induced PSH LLPS in the presence of cages (one-pot) to engage in condensate formation from the initiation of LLPS in a more equilibrated manner. All protein cages with 6His, except HF oligo, which has only partially exposed 6His tags (Fig. S1), were observed inside condensates rather than on surfaces and did not prevent condensate growth (Fig. 1e). The interactions between cages and PSH (electrostatic and 6His-Ni^{2+} binding) might be excessively strong, causing them to phase separate together into the same condensates. Small HF and POK cages even without 6His were also predominantly observed inside condensates, and condensate sizes increased from 10 min to 60 min. HF and POK with their rather small sizes might lack enough surface stabilization energies to remain on PSH condensate surfaces. On the other hand, small coalescence-free PSH condensates were stably formed in the presence of large HF oligo and mi3 without 6His (yellow box) (Fig. 1e and Fig. S2a). HF oligo and mi3 were securely bound on the surface of these small condensates (Fig. S2b).

These data suggest crucial conditions for the synthesis of stable protein condensates. Larger cages were more effective in condensate stabilization, as also suggested by Pickering emulsion theory. More importantly, interactions between protein cages and condensates must be robust enough to prevent coalescence, but these interactions cannot be overly strong, which causes cage penetration into condensates (Fig. 1f). To further validate this synthesis principle, we varied cage-condensate interactions in diverse ways. When the condensate-binding SH3 was additionally fused to HF oligo to enhance binding strength, cages readily penetrated condensates, resulting in enlarged condensates (Fig. 1g). When 6His tags were removed from HF oligo to reduce binding strength, cage binding to surfaces was evidently decreased, once again resulting in enlarged condensates. We also varied electrostatic interactions between mi3 cages and PSH condensates by altering salt concentration. With added salts and thereby reduced electrostatic interactions, mi3 surface binding was dramatically diminished, leading to condensate growth (Fig. 1h). At low salt concentration, with enhanced electrostatic interactions, mi3 cages were found inside condensates and did not function as an interface stabilizer to prevent coalescence.

Synthesis of diverse cage-stabilized protein condensates

We found that cage-condensate interactions could be carefully tuned to obtain a delicate balance for preventing coalescence and avoiding excessive cage penetration. Our next step was to assess the applicability of interfacial protein cages to a broader range of protein condensates with varying properties. First, we examined protein condensates resembling those formed by PSH but with increased fluidity. PS-RL48, featuring an extended linker between PRM-SH3 and 6His, undergoes LLPS, forming positively charged (PSH-like) but highly fluidic condensates (Fig. 2a).[30] Small protein cages readily penetrated fluidic PS-RL48 condensates during LLPS and even to pre-formed condensates (Fig. S3a). Large HF oligo and mi3 with 6His, capable of both electrostatic and 6His-Ni^{2+} binding, also penetrated PS-RL48 condensates, while these cages without 6His only weakly bound to condensate surfaces. All these large cages also failed to prevent coalescence (Fig. 2a and Fig. S3a). These results indicate that optimal stabilization conditions for PS-RL48 condensates are clearly different from those for PSH condensates. In the search for optimal cage-condensate interaction, we first reduced the (electrostatic) condensate binding strength of HF oligo with partial 6His tags by mutating HF into a more neutral form[36] (neu-HF oligo) (Fig. S3b). Although neu-HF oligo slightly penetrated condensates, condensate coalescence was also slightly reduced (Fig. 2a, yellow box). Therefore, we further weakened the binding strength of neu-HF oligo by gradually lowering Ni^{2+} concentration. Although smaller PS-RL48 condensates were formed with reduced [Ni^{2+}], LLPS was also significantly diminished (Fig. 2b). To compensate for weakened LLPS while maintaining low [Ni^{2+}], the crowding agent PEG[37] was added. While high PEG (4%) caused heterogenous cage aggregations, coalescence-free PS-RL48 condensates were stably formed with 1%-2% PEG and low [Ni^{2+}] (Fig. 2b and Fig. S3c). This optimization process illustrates how precise interaction adjustment through protein engineering and binding condition tuning enables the discovery of ideal stabilization conditions for target protein condensates.

We next investigated condensates composed of intrinsically disordered proteins (IDPs), which play a vital role as primary scaffold proteins in cellular LLPS.[38] Protein condensates of LAF[39], a well-known LLPS IDP, were similarly formed by mixing 6His-tagged LAF and Ni^{2+}. The resulting LAF condensates were also highly fluidic (Fig. S4a). Unlike PSH and PS-RL48 condensates, however, designed LAF condensates are slightly negatively charged. Consequently, protein cages without 6His were unable to adsorb to condensate surfaces and stabilize them, regardless of the introduction timing (sequential or one-pot) (Fig. 2c and Fig. S4b). On the other hand, cages such as HF oligo, mi3, and HF with 6His tags effectively adsorbed on LAF condensate and delayed coalescence. However, condensate sizes still slowly but evidently increased, indicating that cage-condensate interactions were not strong enough without electrostatic attractions. To further optimize condensate stabilization, 6His-

Ni^{2+} interactions were strengthened by gradually increasing [Ni^{2+}]. Stable and coalescence-blocked LAF condensates were formed at higher [Ni^{2+}] (100 μM), although excess metal ions (200 μM) caused droplet aggregation (Fig. 2d). Observed stabilization was specific for 6His-Ni^{2+} interactions since condensate binding of mi3 without 6His was not influenced by [Ni^{2+}] increases (Fig. S4c).

Lastly, we explored condensates formed through non-Ni^{2+} mediated LLPS. The phase separable PRM-SH3 motif was tandemly repeated (PRM-SH3-PRM-SH3-6His, PS2H) to enhance the LLPS propensity of the scaffold. PS2H underwent LLPS at a low salt concentration ([NaCl] = 60 mM), without requiring any protein clustering, into highly fluidic and positively charged condensates (Fig. S5a), similar to PS-RL48 condensates. However, unlike PS-RL48 condensates, PS2H condensates were effectively stabilized by large HF oligo and mi3 cages without the need for any cage-condensate binding adjustment (Fig. 2e and Fig. S5b). Small and coalescence-blocked PS2H condensates were formed with HF oligo and mi3, regardless of 6His, due to the absence of Ni^{2+}. Enhanced electrostatic interactions between cages and condensates under the lowered salt concentration likely contribute to this effective stabilization. However, a further increase in cage-condensate interactions by SH3 fusion or [NaCl] decreases (40 mM) caused cage penetration and condensate coalescence (Fig. 2f and Fig. S5b). In addition, small cages still readily penetrated condensates (Fig. S5b), once again highlighting the importance of interfacial cage sizes. In summary, our systematic exploration of various protein condensates under diverse LLPS conditions demonstrates the versatility and adaptability of interfacial protein cages to stabilize protein condensates.

Size-controlled synthesis of cage-stabilized protein condensates

We envisioned that the formation of cage-stabilized protein condensates starts with rapid nucleation and growth, possibly accompanied by early coalescence. Subsequently, protein cages, possessing proper condensate binding strength and sizes, begin to adsorb onto condensate surfaces. The growth of condensates through coalescence halts as the condensates become sufficiently covered by cages. In this scenario, we believed that condensate sizes can be determined by relative quantities of condensates and cages for a given condensate/cage pair (Fig. 3a). At low [cage], the total surface area of early small condensates (before extensive coalescence) is too large to be effectively protected by cages. Consequently, these partially protected condensates continue to fuse into larger ones until the total surface area diminishes enough to be sufficiently covered by cages. On the other hand, at high [cage], even small condensates with a large total surface area can be effectively stabilized by cages.

To control the size of PSH condensates with interfacial HF oligo, the PSH/HF oligo ratio was

extensively varied. The size diagram of confocal microscope images shows HF oligo-PSH condensates with sizes ranging from nano- to micro-scale (Fig. 3b). At a fixed [PSH], the condensate size decreased as [HF oligo] increased, and at the fixed [HF oligo], the condensate size increased as [PSH] increased. PSH condensates as large as 3 μm were synthesized with 50 μM PSH (Fig. S6a). Due to the optical resolution limit, the sizes of small condensates were analyzed using negative-stained TEM (Fig. 3c). With varying [HF oligo] (from 10 nM to 40 nM) at a fixed [PSH] (20 μM), the synthesized condensate sizes ranged from approximately 150 nm to 860 nm on average with high homogeneity (Fig. 3d). Further increases in [HF oligo] caused heterogeneous aggregation of condensates and excess cages, suggesting that ~100 nm might be the size limit of HF oligo-stabilized PSH condensates (Fig. S6b-d).

Condensate formation yield was assessed by separating condensates from the surrounding solution through centrifugation. Most PSH and HF oligo were included in condensates, offering an excellent synthesis yield (Fig. 3e). Moreover, when [HF oligo] increased at a fixed [PSH], the PSH quantity in cage-stabilized condensates remained constant while surface-bound HF oligo increased (Fig. 3f). These data support our cage-stabilization mechanism, where small condensates, with a large total surface area, are covered by more cages (Fig. 3a). This also indicates that condensate coalescence and subsequent size control by cages do not influence LLPS propensity.

By altering [condensate]/[cage] ratios, we were also able to extensively vary the sizes of all synthesized condensates such as PSH/mi3, PS-RL48/HF oligo, and LAF/mi3 condensates with high synthesis yields (Fig. 3g & Fig. S7). Many factors such as stabilization energy, the kinetics of LLPS and condensate-cage binding, and condensate densities, likely influence condensate sizes. Nonetheless, size control through [condensate]/[cage] variations was highly consistent and reliable, without requiring time-dependent kinetic manipulation. Moreover, the search for conditions to reach target sizes was straightforward, with predictable size changes.

The structure of cage-stabilized protein condensates

We next investigated the structural intricacies of synthesized protein condensates, placing particular emphasis on the distribution of interfacial cages around the condensates. The classical Pickering-type emulsification theory predicts the localization of Pickering agents to form a monolayer at the phase boundary.[25] The core-shell structures of micro-sized protein condensates were visualized using confocal microscopy imaging and subsequent Z-stacking (Fig. 4a). However, the inherent resolution limit of light microscopy prevented confirmation of shell formation by cages on smaller condensates, and precise cage locations at the condensate interfaces remained unknown. To address this limitation,

we employed transmitted electron microscopy (TEM)-based methods, enabling the visualization of individual protein cages. Negative-stained TEM images of various protein condensates clearly indicated that protein cages were densely located on condensates (Fig. 4b & Fig. S8a). Nevertheless, these projection TEM images, with heavy metal staining, still do not provide information on the relative positions of protein cages on condensate surfaces.

We next employed cryo-EM, which has the potential to distinguish different electron density patterns of protein condensates and cages without heavy metal staining and sample drying. For cryo-EM analysis, protein condensates must be trapped in an ice layer, which needs to be thinner than 100-200 nm for effective electron transmission across the sample.[40] While typical protein condensates grow rapidly to micro-size, our stabilized condensates can be controlled in size down to ~100 nm. Small mi3-stabilized condensates were prepared and successfully trapped in thin ice layers for cryo-EM analysis. Representatively, rigid PSH condensates and disordered LAF condensates with mi3 were examined. Surface-bound mi3 cages and protein condensates with high electron densities were clearly visualized for both PSH and LAF condensates (Fig. 4c & Fig. S8b,c). Interfacial mi3 cages were fairly uniformly located on the condensate surface, suggesting mi3 monolayer structures on the condensates.

We further extended cryo-EM to electron tomography (ET) to fully reconstruct 3D structures of cage-stabilized condensates. A series of tilting cryo-EM images were aligned and used to reconstruct tomograms (Fig. 4d & Fig. S9). These tomograms were then segmented to create a 3D volume model, with GFP-fused mi3 represented as a 25 nm-sized sphere. The 3D volume model clearly revealed a highly packed monolayer shell of mi3 on a LAF condensate (Fig. 4e). These structural data strongly support our synthesis principles of cage-stabilized protein condensates. PSH condensates were also uniformly covered with a mi3 monolayer (Fig. S10a). In cryo-ET structures, many condensates were noticeably squeezed into ellipsoidal shapes with ~150 nm thicknesses. We suspect that the surface tension at the air-water interface[41] exerted upon condensate embedment in a thin water layer might have caused the squeezing of liquidic protein condensates that are larger than the water layer. In fact, small condensates (~100 nm) mostly retained their spherical shapes (Fig. 4e).

To further confirm the absence of cages inside condensates, tomograms were obtained with intentionally inserted protein cages. HF-6His cages readily penetrated PSH condensates (Fig. 1c). A small amount of HF-6His was added during the synthesis of mi3-PSH condensates. Smaller HF cages were clearly observed in tomograms, while all mi3 cages were on the condensate boundary (Fig. 4f). Close examination of tomograms suggested that interfacial mi3 cages maintained a relatively consistent contact angle with condensate interfaces (Fig. 4g and Fig. S10b). The cages were only

slightly buried in the condensates. Pickering agents having a contact angle lower than 90° on a highly curved interface is a commonly known feature in Pickering emulsion.[22] However, we cannot rule out the possibility that condensates have protein brush-like surfaces,[42] which are difficult to visualize due to low and sporadic electron densities. Surface protein brushes will further influence cage interactions on condensate surfaces. Interestingly, the contact angles were slightly smaller on rigid and more dense PSH condensates than on LAF condensates (Fig. 4g and Fig. S10b). It is also noteworthy that mi3 coverages on PSH condensates were clearly less complete than on LAF condensates (Fig. 4h). It is possible that complete interface covering might not be required to block coalescence for certain condensates and LLPS conditions.

Dynamic behaviors of cage-stabilized protein condensates

Finally, we examined whether surface-covered protein condensates retain dynamic properties, such as the ability to selectively exchange materials with the outside. Identical condensates were separately prepared with different dye labels (Cy5 and Cy3) for all examined condensates (PSH, PS-RL48, LAF, PS2H) and mixed. For fluidic condensates (PS-RL48, LAF, PS2H), the two dyes were homogeneously distributed in all condensates (Fig. 5a and Fig. S11a,b), indicating dynamic scaffold protein exchanges between condensates without coalescence. On the other hand, scaffold exchange was not observed for rigid PSH condensates (Fig. 5a and Fig. S11c). Protein exchanges between fluidic condensates were gradual but fairly rapid, reaching new equilibrium states before 10 min after mixing, while the composition of PSH condensates remained mostly unchanged even after 60 min incubation (Fig. S11a-c). In the absence of cages, only PSH condensates did not exchange their scaffold proteins (Fig S11d), indicating that condensate characteristics were well preserved even after dense wrapping with interfacial cages.

We next investigated the selective recruitment of outside materials, one of the unique features of condensate materials. Negatively charged DNA was well recruited into positive PSH and PS-RL48 condensates but not into negative LAF condensates (Fig. 5b). 6His-tagged mCherry was well recruited into all Ni^{2+}-coordinated condensates except rigid PSH condensates. These biomolecules could also be strongly encapsulated in condensates by simply adding them during cage-stabilized condensate synthesis (Fig. S12a). For more controlled, interaction-driven recruitment, antibody-binding protein G was introduced to PSH condensates.[43] Antibodies were effectively encapsulated in cage-stabilized condensates only with fused protein G (Fig. 5c and Fig. S12b). The dynamic and reversible nature of condensates is clearly distinct from similarly dense but irreversible protein aggregates. When extra

scaffold proteins were introduced to stabilized condensates, condensate sizes readily increased for all scaffolds (Fig. 5d and Fig. S12c), reaching new reversible states. In contrast, the structures remained unaltered by protein cage addition since the condensates were already fully stabilized. This dynamic behavior offers another potent route to fine-tune the size of condensates.

Condensates can also be disassembled by changing the solution conditions to discourage LLPS. For instance, concentration dilution gradually dissolved fluidic PS-RL48 condensates with interfacial cages (Fig. S13a). Interestingly, rigid PSH condensates exhibited unexpectedly high resistance against various external perturbations. The cage-coated structures remained intact after dilution (or even full buffer exchange by dialysis) and at various temperatures (Fig. S13b). Therefore, cage-stabilized PSH condensates could be isolated from the synthesis solution (Fig. 5e) and also further separated based on their sizes using sucrose gradient centrifugation (Fig. S13c). PSH condensates could still be disassembled when key interactions were disturbed, such as by metal chelators to reverse 6His-Ni^{2+} coordination. These data indicate that the resistance of cage-stabilized condensates against external changes is mainly governed by the dynamicity of core condensates. Therefore, the stability of our synthesized condensates might be controllable by manipulating condensation forces. In fact, when long DNAs were recruited into fluidic PS-RL48 condensates, the condensate size was notably reduced (Fig. S13d). Many PS-RL48 proteins could assemble around DNAs, which might lead to enhanced condensation and a size decrease. Cage-stabilized PS-RL48 condensates became significantly less fluidic upon DNA recruitment, and protein exchanges between condensates were also vastly slowed (Fig. 5f and Fig. S13e). These DNA-inserted condensates were highly resistant to concentration dilution. Scaffold clustering enhancement can be a selective, reversible, and physiological strategy to increase the stability of cage-stabilized condensates.

Interfacial cages not only contribute to the structural integrity but also impart additional functional features to our condensate materials. To demonstrate this concept, we investigated how HF cages on condensates influence condensate behaviors. HF preferably recognizes and internalizes cancer cells through transferrin receptors.[44] We prepared nano-sized HF oligo-covered PSH condensates co-assembled with cargo DNAs or antibodies. These were then applied to HeLa cells. The signals from HF, PSH, and the cargo components were all detected inside the cells, affirming the cellular uptake of the entire condensates (Fig. 5g). In contrast, free DNAs or antibodies could not penetrate the cells. Notably, when mixtures of HF oligo, PSH, and cargo were directly applied to cells without prior condensate formation (excluding Ni^{2+}), only HF was observed entering the cells (Fig. S13f).

Conclusions

In this study, we present a reliable approach for synthesizing stable protein condensates with sustained integral structures, additional boundary functions, and well-defined sizes ranging from micro- to nanoscale dimensions. Routes to find optimal interfacial protein cages and LLPS conditions for given condensates are straightforward, primarily adjusting interactions between cages and condensate-forming proteins. Precise and systematic adjustment was possible with fully protein-based interactions. We envision that other biopolymers with defined binding moieties and sizes could also be developed as interfacial stabilizers. The synthesis is both simple and efficient as a one-pot assembly with high overall yields. Size control, achieved by altering [condensate]/[cage] ratios, is also undemanding. We believe that our method is reachable to many researchers, opening avenues for diverse exploration and applications of protein condensates as novel biomaterials.

We synthesized cage-stabilized protein condensates as small as 100–150 nm with interfacial cages of approximately 30 nm. Determining factors for this size limit (e.g., cage size, LLPS speed, and condensate liquidity) are not yet clear, requiring further investigation. Nevertheless, our ability to stably isolate these small condensates enabled the first 3D structure visualization of protein condensates with interfacial entities using cryo-ET. Interfacial cages are only slightly buried in condensates with contact angles between 40 and 80 degrees, and PSH condensates could be stabilized even without full cage coating. We believe that our strategy can be used to reveal unknown structural information on diverse biomolecular condensate-related activities. For example, we plan to investigate changes in interfacial and internal structures by monitoring stabilized protein condensates subjected to external stimuli. It will be also interesting to encapsulate specific biomolecules inside cage-stabilized condensates and visualize their structures under condensate environments using cryo-ET.

Our work on condensate surface stabilization will also significantly contribute to understanding mechanisms that modulate cellular MLO sizes. P granules in Caenorhabditis elegans were similarly stabilized by protein clusters[26], and stress granules sizes were also influenced by surface-bound protein-RNA clusters[45]. Surface accumulated RNAs could also stabilize protein condensates.[46,47] We demonstrated that this stabilization mechanism is not a rare phenomenon limited to certain condensates but rather universally applicable and tunable. Our cryo-ET data provide clear structural evidence for this Pickering-type emulsification of protein condensates. Future work will focus on elucidating the mechanism of action of interfacial entities on protein condensates in more detail. In addition, with fully protein-based interfacial entities, our strategy could be further developed to manipulate MLOs in cells.

While this study establishes a foundation for the development of dynamic and functional condensate

materials, tailoring methods need further refinement for diverse applications in biotechnology and medicine. For example, it will be necessary to develop strategies to encapsulate non-phase separable cargos, such as biopharmaceuticals, in high quantities, and to design new interfacial cages suitable for these cargo-heavy condensates. Additionally, it is crucial to develop methods for further stabilizing condensate assembly structures, as cage-covered condensates can be disassembled when LLPS driving forces or equilibrium states are disrupted. Additional clustering of condensate-forming proteins can be a potent approach, as demonstrated by the fact that fluidic PS-RL48 condensates became more resistant against equilibrium shift by DNA recruitment and subsequent PS-RL48 clustering around DNA.

Methods

Preparation of engineered proteins. All genes encoding indicated proteins were cloned into the pET-21a(+) plasmid (Novagen). Cloned plasmids were transformed into BL21(DE3), and the cells were grown in LB until the A600 reaches 0.6~0.8. 1 mM IPTG (LPS solution) was added, and the cells were incubated overnight at 20 °C. Protein expressing cells were harvested by centrifugation and sonicated. The cell lysates were centrifuged at 12000 rpm for 15 min. 6His-tagged scaffold proteins and GFP-6His were purified by using Ni-IDA resins (BioProgen). To remove residual nickel ions in purified proteins, 500 μM EDTA was added to the purified protein eluents, and overnight dialysis was performed twice in 1×PBS (KH_2PO_4 1.1 mM, NaH_2PO_4 3 mM, NaCl 160 mM). For HF and mi3 variants, supernatants were heated at 60 °C for 10 min before being purified using size exclusion chromatography (SEC) with a Sepacryl S-300 column (buffer: Tris 50 mM, NaCl 150 mM, pH 7.2). POK variants were also purified by SEC, but without heat treatment. Protein cages were then dialyzed in 1×PBS. HF oligos were prepared as previously described.[35] In brief, Z_E fused HF and Z_R fused HF were mixed at a 1 : 10 ratios for 3 h, then mixtures were purified using Ni-IDA resins. 500 μM EDTA were added to the purified protein solution to remove free nickel ions, and the solution was dialyzed twice in 1×PBS.

Fluorescent dye labeling of proteins. Proteins were tagged using cyanine 3 (Cy3) or 5 (Cy5) N-hydroxysuccinimide (NHS) ester (Lumiprobe). Protein samples were conjugated with cyanine NHS ester at a 1:1 protein-to-dye ratio. After incubating for 2 h at 25°C, dye-conjugated proteins were purified using PD-10 desalting columns (SephadexTM G-25 M, GE Healthcare).

Protein phase separation and confocal microscopy imaging. 6His tagged scaffold proteins were filtered (0.2 μm DISMIC-25CS, Advantec) and stored in 1×PBS before LLPS. Protein condensates were formed by adding $NiCl_2$ to scaffold proteins under indicated buffer conditions. PS2H condensates were generated by mixing scaffold solution (in 1× PBS) and NaCl-free phosphate buffer (KH_2PO_4 1.1

mM, NaH_2PO_4 3 mM) to meet the specified scaffold and NaCl concentrations. After 2 min incubation, samples were transferred to 10% BSA-passivated μ-slide 18 well (ibidi). Condensates were analyzed by the A1R HD25 confocal microscope (Nikon) using a 60×/1.40 Apochromat Lambda D Oil objective lens. Fluorescent images were taken at 488 nm for GFP-fused protein cages, 561 nm for Cy3-tagged proteins, and 647 nm for Cy5-tagged proteins. The images were processed and analyzed using the NIS Elements software (Nikon). Confocal Z-stack 3D images were obtained in an agarose gel to prevent condensate motions.

Fluorescence Recovery After Photobleaching assay (FRAP). Photobleaching was performed on circular regions of protein droplets, with region of bleaching (ROB) areas accounting for less than 10% of the total droplet area. Cy3- or Cy5-tagged protein droplets were bleached using a 561 nm or 647 nm laser, respectively. Time-lapse images were captured over a 10 sec period. The intensities of ROB, background (BG), and reference (REF) regions were measured using NIS Elements. Recovery curves were plotted $(I_{ROB} - I_{BG})/(I_{REF} - I_{BG})$ (I_X: Intensity of X region.) against time. $(I_{ROB} - I_{BG})/(I_{REF} - I_{BG})$ before photobleaching was set to 1 and $(I_{ROB} - I_{BG})/(I_{REF} - I_{BG})$ right after photobleaching was set to 0 as previously described.[30] The normalized fluorescence intensity (nFI) was fitted to a simple exponential model, $nFI(t) = b(1 - e^{-at})$, using Origin.

Synthesis of protein cage-stabilized protein condensates. For sequential cage stabilization, protein condensates were formed for 2 min under given conditions (e.g., [PSH]/[Ni^{2+}]: 50/50 μM, [PS-RL48]/[Ni^{2+}]: 30/30 μM, [LAF]/ [Ni^{2+}]: 20/20 μM, [PS2H]/[NaCl]: 50 μM/60 mM), followed by the addition of various protein cages (final concentrations: 50 μg/mL). For one-pot synthesis of protein cage-stabilized condensates, $NiCl_2$ was introduced (or mixing NaCl-free phosphate buffer for PS2H) to scaffold/cage mixtures to induce LLPS. Synthesis procedures were optimized by adjusting total protein concentrations, scaffold/cage ratios, crowding agent PEG 8000 (LPS solution), salt concentrations, and applied protein cages. To measure condensate formation yields, synthesized condensates were centrifuged at 14000×g for 30 min. The resulting condensate pellets were resuspended and applied to 15% SDS PAGE denaturing gels. Gels were stained with Coomassie Blue and imaged by ChemiDoc MP (Biorad).

Negative-stained Transmission Electron Microscopy (TEM). Protein samples (0.03 mg/mL) were adsorbed on a glow-discharged carbon-coated grid (200 mesh, TED PELLA, INC) for 2 min. The grid was washed with distilled water twice. To achieve negative staining, the grid was treated with 2% uranyl acetate for 1 min and then air-dried for 10 min. The samples were examined using a Tecnai G2 F30 S-Twin 300 kV TEM. Images were acquired at various magnifications (×2,900, ×3,900, ×5,000, ×25,000, or ×35,000), depending on sample sizes.

Size distribution analysis. Size distribution curves were founded using Origin employing statistics from condensates acquired in TEM or confocal images. Images were converted to binary format using the ImageJ software, and assuming that the condensates are circular, the diameters were computed by inverting the area.

Cryo-EM/ET sample preparation. Quantifoil Cu 400-mesh R1.2/1.3 holey carbon grids (Quantifoil Micro Tools GmbH, Germany) were glow-discharged (0.38mbar/15mA/30 sec). Grids were then loaded with 3-4 μL of condensate sample solution, blotted, and plunge-frozen in liquid ethane using Vitrobot (Thermo Fisher Scientific, USA). For certain LAF-associated condensate samples, 10 nm BSA-treated gold nanoparticles were introduced as a fiducial marker. Grids were then stored in liquid nitrogen until they were imaged.

Cryo-electron tomography (cryo-ET) and tomogram reconstruction. Vitrified sample grids were loaded onto either Titan Krios (300 kV) or Titan Glacios (200 kV) TEM (Thermo Fisher Scientific, USA). The tilt series were acquired using Tomography software (Thermo Fisher Scientific, USA). The tilt series were acquired over a tilt range of -60° to 60° with an increment of 2°, while limiting the total cumulative electron dose under 120e/Å^2. Nominal magnification was 53k× with a pixel size of 0.24 nm. Tilt series images were aligned and reconstructed using IMOD.[48,49] With samples containing gold fiducial markers, cross-correlation and fiducial marker tracking were used to align the tilt series. Samples without gold fiducial markers, on the other hand, cross-correlation and patch-tracking were used in an alignment process. Aligned tilt series were then used to reconstruct tomograms. All tomograms were reconstructed with the SIRT (Simultaneous Iterative Reconstruction Technique) algorithm, with an iteration number of 20.

For visual representation, image filters were applied using ImageJ software.[50] The segmentation process was done using the 3dmod software in an IMOD package. The location of surface cages (GFP-fused mi3) was manually determined to build 3D volume models. Cages were visualized as 25 nm spheres (the size of mi3), since GFPs fused on mi3 were not clearly observed in cryo-EM images. Contact angles were measured by drawing a line connecting two intersection points at the contact site of mi3 on a condensate surface and another line, tangential to the cage circle at these intersection points. Note that measured contact angles might have been understated, since GFP-fused mi3 is probably larger than 25 nm.

Client recruitment. mCherry-6His (2 μM) and Cy5-DNA (25 nM) were treated to pre-formed cage-stabilized condensates. For one-pot recruitment, these biomolecules were mixed together with scaffolds and protein cages prior to Ni^{2+}-induced LLPS. For recruiting Human IgG (Sigma), a mixture of 48 μM of PSH and 2 μM of Protein G-PSH were used as scaffold proteins. Scaffolds, 0.1 μM of Cy5-tagged HIgG, and HF oligo mixtures were incubated for 5 min before Ni^{2+}-triggered LLPS.

Encapsulation efficacies were investigated by gel electrophoresis, where condensates (pellets) and non-participants (supernatants) were separated through centrifugation (at 14000×g for 30 min), then loaded onto denaturing gels. Fluorescence signals of DNA and IgG were investigated by ChemiDoc MP (Biorad).

Sucrose density gradient centrifugation. Sucrose solutions were prepared in 10% increments, ranging from 10% to 60%. A discontinuous sucrose gradient column was built up in polypropylene tubes (Beckman), with 2 mL of each sucrose solution layered from bottom to top, followed by 1 mL of cage-stabilized protein condensate mixtures transferred to the highest layer of the sucrose gradient column. Samples were centrifuged (Optima XE-90, Beckman) at 20,000×g for 20 min at 4°C using the SW41Ti rotor. Afterwards, each layer was carefully isolated, a 1 mL aliquot from the top of the gradient.

Cell experiments. HeLa cells in Dulbecco's Modified Eagles' medium (DMEM, Gibco) supplemented with 10% fetal bovine serum (HyClone) and 1% penicillin–streptomycin (Gibco) were seeded on an 8-well plate (ibidi) (1×10^4 cells per well) and incubated at 37 °C under 5% CO_2 in a humidified atmosphere for 24 h. DMEM were removed and washed twice with cold Dulbecco's phosphate-buffered saline (DPBS) before being treated with 100 nM of DNA (21 bp), DNA encapsulated PSH/HF oligo-stabilized condensates, 100 nM of HIgG, and HIgG encapsulated PSH/HF oligo-stabilized condensates. HeLa cells were then further incubated at 37 °C for 4h, followed by two washes with DPBS. A confocal microscope was used to acquire fluorescent images of HeLa cells.

Acknowledgements

This work is supported by the National Research Foundation of Korea (NRF) grant (2023R1A2C2005183) and by the Basic Research Laboratory (BRL) Program (2022R1A4A1033471) funded by the Korea government (MSIT). We thank Jinwoo Kim and KARA (KAIST Analysis center for Research Advancement) for assisting EM analysis.

Author contributions

H.J.O. and Y.L. designed, conducted and analyzed experiments. H.H. and J.Y.K. helped structural analysis using cryo-EM and -ET. K.H. and H.C. initiated the project. Y.J., H.J.O., and Y.L. wrote the manuscript with help from all authors. Y.J. designed the project and supervised the work.

Additional information

Supplementary information is available.

Competing interests

The authors declare no competing interests.

References

1. Brangwynne, C.P., Tompa, P. & Pappu, R.V. Polymer physics of intracellular phase transitions. *Nat. Phys.* **11**, 899-904 (2015).
2. Shin, Y. & Brangwynne, C.P. Liquid phase condensation in cell physiology and disease. *Science* **357**, eaaf4382 (2017).
3. Banani, S.F., Lee, H.O., Hyman, A.A. & Rosen, M.K. Biomolecular condensates: organizers of cellular biochemistry. *Nat. Rev. Mol. Cell Biol.* **18**, 285-298 (2017).
4. Alberti, S., Gladfelter, A. & Mittag, T. Considerations and Challenges in Studying Liquid-Liquid Phase Separation and Biomolecular Condensates. *Cell* **176**, 419-434 (2019).
5. Boeynaems, S. et al. Protein Phase Separation: A New Phase in Cell Biology. *Trends Cell Biol.* **28**, 420-435 (2018).
6. Alberti, S. Phase separation in biology. *Curr. Biol.* **27**, R1097-R1102 (2017).
7. Ma, Q. et al. Cell-Inspired All-Aqueous Microfluidics: From Intracellular Liquid-Liquid Phase Separation toward Advanced Biomaterials. *Adv. Sci. (Weinh)* **7**, 1903359 (2020).
8. Villegas, J.A., Heidenreich, M. & Levy, E.D. Molecular and environmental determinants of biomolecular condensate formation. *Nat. Chem. Biol.* **18**, 1319-1329 (2022).
9. Abbas, M., Lipinski, W.P., Wang, J. & Spruijt, E. Peptide-based coacervates as biomimetic protocells. *Chem. Soc. Rev.* **50**, 3690-3705 (2021).
10. Son, J. & Jung, Y. Lipid coated protein condensates as stable protocells with selective uptake abilities for biomolecules. *Chem. Sci.* **13**, 11841-11848 (2022).
11. Iwata, T. et al. Liquid Droplet Formation and Facile Cytosolic Translocation of IgG in the Presence of Attenuated Cationic Amphiphilic Lytic Peptides. *Angew. Chem. Int. Ed.* **60**, 19804-19812 (2021).
12. Sun, Y. et al. Phase-separating peptides for direct cytosolic delivery and redox-activated release of macromolecular therapeutics. *Nat. Chem.* **14**, 274-283 (2022).
13. Peeples, W. & Rosen, M.K. Mechanistic dissection of increased enzymatic rate in a phase-separated compartment. *Nat. Chem. Biol.* **17**, 693-702 (2021).
14. Liu, J., Zhorabek, F., Dai, X., Huang, J. & Chau, Y. Minimalist Design of an Intrinsically Disordered Protein-Mimicking Scaffold for an Artificial Membraneless Organelle. *ACS Cent. Sci.* **8**, 493-500 (2022).
15. Le Ferrand, H., Duchamp, M., Gabryelczyk, B., Cai, H. & Miserez, A. Time-Resolved Observations of Liquid-Liquid Phase Separation at the Nanoscale Using in Situ Liquid Transmission Electron Microscopy. *J. Am. Chem. Soc.* **141**, 7202-7210 (2019).

16. Ranganathan, S. & Shakhnovich, E.I. Dynamic metastable long-living droplets formed by sticker-spacer proteins. *Elife* **9**, e56159 (2020).
17. Heuer-Jungemann, A. et al. The Role of Ligands in the Chemical Synthesis and Applications of Inorganic Nanoparticles. *Chem. Rev.* **119**, 4819-4880 (2019).
18. McClements, D.J. & Jafari, S.M. Improving emulsion formation, stability and performance using mixed emulsifiers: A review. *Adv. Colloid Interface Sci.* **251**, 55-79 (2018).
19. De, S., Malik, S., Ghosh, A., Sahab, R. & Saha, B. A review on natural surfactants. *RSC Adv.* **5**, 65757-65767 (2015).
20. Kelley, F.M., Favetta, B., Regy, R.M., Mittal, J. & Schuster, B.S. Amphiphilic proteins coassemble into multiphasic condensates and act as biomolecular surfactants. *Proc. Natl. Acad. Sci. USA* **118**, e2109967118 (2021).
21. Linsenmeier, M. et al. The interface of condensates of the hnRNPA1 low-complexity domain promotes formation of amyloid fibrils. *Nat. Chem.* **15**, 1340-1349 (2023).
22. Albert, C. et al. Pickering emulsions: Preparation processes, key parameters governing their properties and potential for pharmaceutical applications. *J. Control. Release* **309**, 302-332 (2019).
23. Yang, Y. et al. An Overview of Pickering Emulsions: Solid-Particle Materials, Classification, Morphology, and Applications. *Front Pharmacol.* **8**, 287 (2017).
24. Xiao, M., Xu, A., Zhang, T. & Hong, L. Tailoring the Wettability of Colloidal Particles for Pickering Emulsions via Surface Modification and Roughness. *Front. Chem.* **6**, 225 (2018).
25. Gonzalez Ortiz, D., Pochat-Bohatier, C., Cambedouzou, J., Bechelany, M. & Miele, P. Current Trends in Pickering Emulsions: Particle Morphology and Applications. *Engineering* **6**, 468-482 (2020).
26. Folkmann, A.W., Putnam, A., Lee, C.F. & Seydoux, G. Regulation of biomolecular condensates by interfacial protein clusters. *Science* **373**, 1218-1224 (2021).
27. Cochard, A. et al. RNA at the surface of phase-separated condensates impacts their size and number. *Biophys. J.* **121**, 1675-1690 (2022).
28. Binks, B.P. Particles as surfactants—similarities and differences. *Curr. Opin. Colloid Interface Sci.* **7**, 21-41 (2002).
29. Levine, S., Bowen, B.D. & Partridge, S.J. Stabilization of emulsions by fine particles II. capillary and van der Waals forces between particles. *Colloids and Surfaces* **38**, 345-364 (1989).
30. Hong, K., Song, D. & Jung, Y. Behavior control of membrane-less protein liquid condensates with metal ion-induced phase separation. *Nat. Commun.* **11**, 5554 (2020).
31. Valenti, L.E., De Pauli, C.P. & Giacomelli, C.E. The binding of Ni(II) ions to hexahistidine as

a model system of the interaction between nickel and His-tagged proteins. *J. Inorg. Biochem.* **100**, 192-200 (2006).

32. Jozic, D., Kaiser, J.T., Huber, R., Bode, W. & Maskos, K. X-ray structure of isoaspartyl dipeptidase from E.coli: a dinuclear zinc peptidase evolved from amidohydrolases. *J. Mol. Biol.* **332**, 243-256 (2003).
33. Jutz, G., van Rijn, P., Santos Miranda, B. & Boker, A. Ferritin: a versatile building block for bionanotechnology. *Chem. Rev.* **115**, 1653-1701 (2015).
34. Hsia, Y. et al. Design of a hyperstable 60-subunit protein dodecahedron. [corrected]. *Nature* **535**, 136-139 (2016).
35. Oh, H.J. & Jung, Y. High order assembly of multiple protein cages with homogeneous sizes and shapes via limited cage surface engineering. *Chem. Sci.* **14**, 1105-1113 (2023).
36. Kunzle, M., Eckert, T. & Beck, T. Binary Protein Crystals for the Assembly of Inorganic Nanoparticle Superlattices. *J. Am. Chem. Soc.* **138**, 12731-12734 (2016).
37. Rivas, G. & Minton, A.P. Macromolecular Crowding In Vitro, In Vivo, and In Between. *Trends Biochem. Sci.* **41**, 970-981 (2016).
38. Abyzov, A., Blackledge, M. & Zweckstetter, M. Conformational Dynamics of Intrinsically Disordered Proteins Regulate Biomolecular Condensate Chemistry. *Chem. Rev.* **122**, 6719-6748 (2022).
39. Elbaum-Garfinkle, S. et al. The disordered P granule protein LAF-1 drives phase separation into droplets with tunable viscosity and dynamics. *Proc. Natl. Acad. Sci. USA* **112**, 7189-7194 (2015).
40. Saibil, H.R. Cryo-EM in molecular and cellular biology. *Mol. Cell.* **82**, 274-284 (2022).
41. Liu, N. & Wang, H.W. Better Cryo-EM Specimen Preparation: How to Deal with the Air–Water Interface? *J. Mol. Biol.* **435**, 167926 (2023).
42. Wang, J., Devarajan, D.S., Nikoubashman, A. & Mittal, J. Conformational Properties of Polymers at Droplet Interfaces as Model Systems for Disordered Proteins. *ACS Macro Lett.* **12**, 1472-1478 (2023).
43. Sjöbring, U., Björck, L. & Kastern, W. Streptococcal protein G. Gene structure and protein binding properties. *J. Biol. Chem.* **266**, 399-405 (1991).
44. Li, L. et al. Binding and uptake of H-ferritin are mediated by human transferrin receptor-1. *Proc. Natl. Acad. Sci. USA* **107**, 3505-3510 (2010).
45. Garcia-Jove Navarro, M. et al. RNA is a critical element for the sizing and the composition of phase-separated RNA-protein condensates. *Nat. Commun.* **10**, 3230 (2019).
46. Hampoelz, B. et al. Nuclear Pores Assemble from Nucleoporin Condensates During Oogenesis.

Cell **179**, 671-686 (2019).

47. Tauber, D. et al. Modulation of RNA Condensation by the DEAD-Box Protein eIF4A. *Cell* **180**, 411-426 (2020).
48. Kremer, J.R., Mastronarde, D.N. & McIntosh, J.R. Computer visualization of three-dimensional image data using IMOD. *J. Struct. Biol.* **116**, 71-76 (1996).
49. Mastronarde, D.N. & Held, S.R. Automated tilt series alignment and tomographic reconstruction in IMOD. *J. Struct. Biol.* **197**, 102-113 (2017).
50. Schindelin, J. et al. Fiji: an open-source platform for biological-image analysis. *Nat. Methods* **9**, 676-682 (2012).

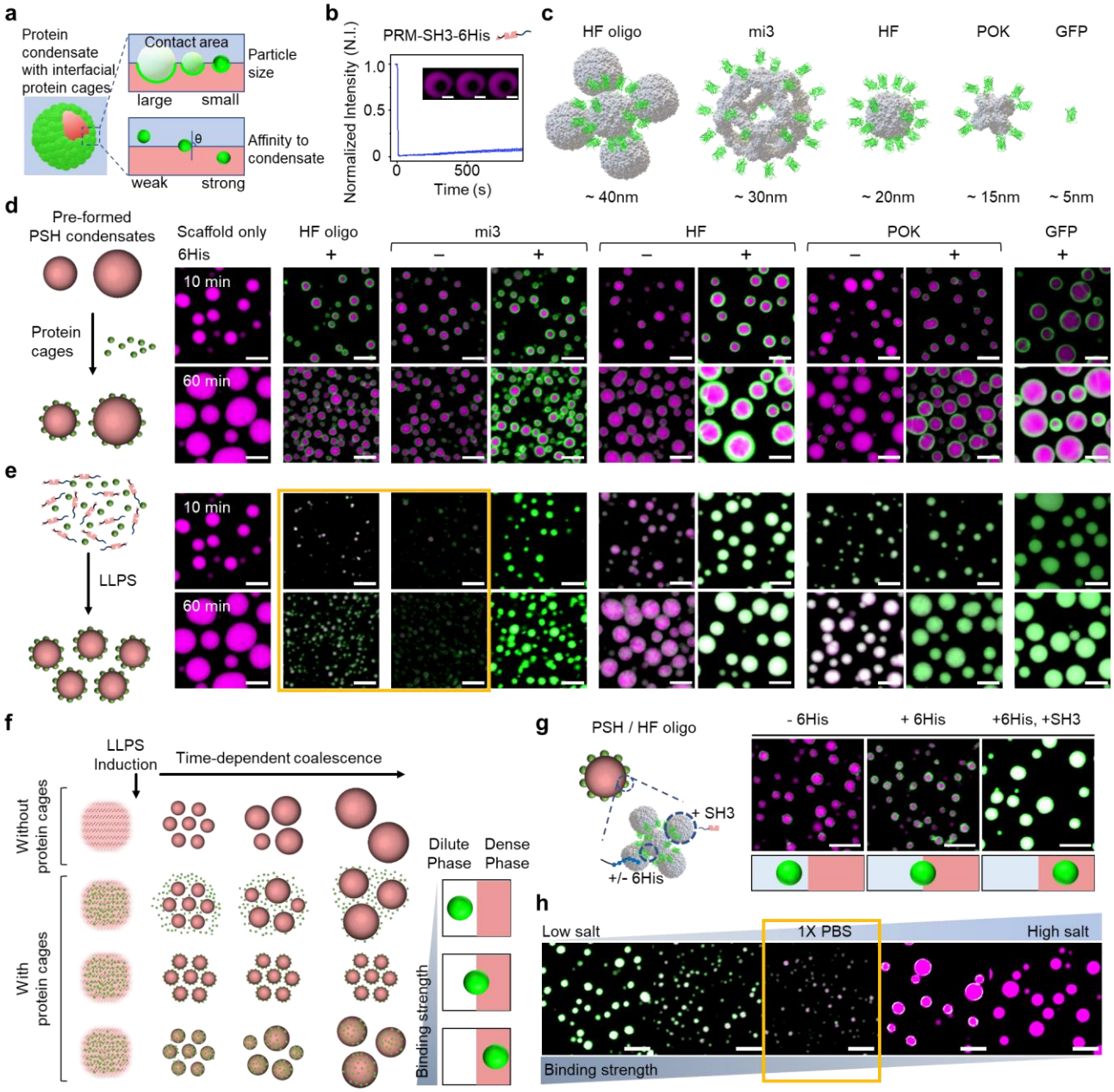

Fig. 1 | Synthesis of surface-stabilized protein condensates with interfacial protein cages. a, Schematic diagram of surface-stabilized (coalescence-free) protein condensates with interfacial protein cages featuring optimized cage size and affinity to condensates . **b,** FRAP recovery profile and confocal images of bleached PSH (magenta) condensates. **c,** Schematic structures of designed GFP (green)-fused interfacial protein cages. The approximate size of each cage is indicated below. **d,** Sequential introduction (schematically expressed left) of HF oligo, mi3, HF, POK, and monomeric GFP with (+) or without (-) 6His to pre-formed PSH condensates. Confocal images of PSH condensates (magenta) without (scaffold only) or with added protein cages (green) after 10- and 60-min incubations are presented. **e,** Confocal images of PSH condensates (magenta) phase separated in the presence of protein cages (one-pot assembly). Surface-stabilized (coalescence-free) protein condensate images are indicated with a yellow box. **f,** Schematics of the synthesis principles of surface-stabilized protein condensates with interfacial protein cages, depending on cage-condensate binding strengths. **g,** Binding strength variation between HF oligo and PSH by removing 6His (weaker) or adding SH3

(stronger) for HF oligo. Confocal images of PSH condensates with HF oligo variants are presented. **h,** Confocal images of mi3-treated PSH condensates at different salt concentrations. Optimally stabilized condensates are indicated with a yellow box. All scale bars, 5 μm.

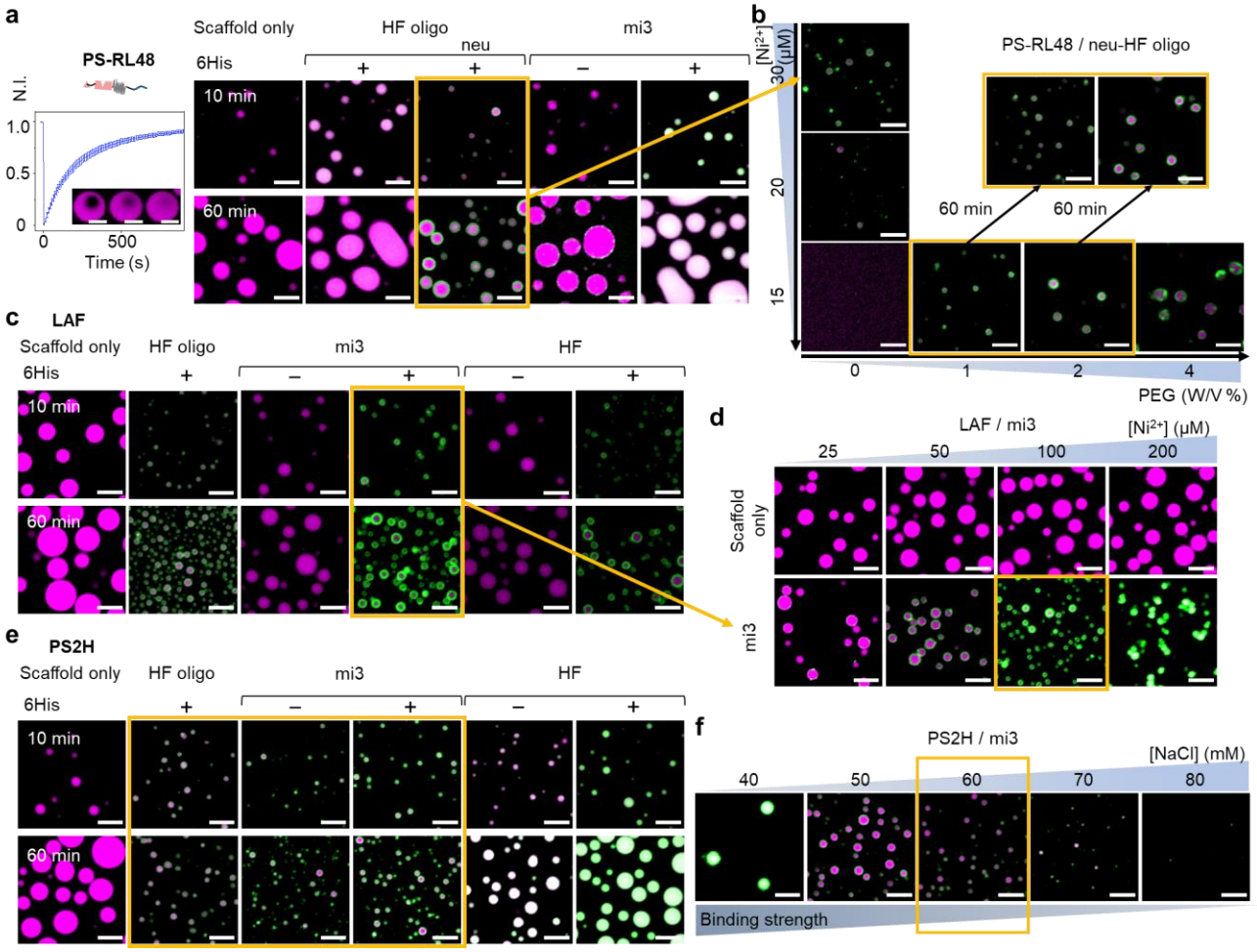

Fig. 2 | Surface stabilization for diverse fluidic protein condensates. a, Confocal images of fluidic PS-RL48 condensates (FRAP data shown left, magenta), phase separated in the presence of indicated protein cage variants (green) (one-pot assembly), after 10- and 60-min incubation. Images for PS-RL48 condensates with neu-HF oligo that has undergone additional optimization (a yellow arrow) are marked with a yellow box. **b,** Confocal images of neu-HF oligo-treated PS-RL48 condensates with systematically varied interaction strengths between neu-HF oligo and PS-RL48. $[Ni^{2+}]$ was decreased to reduce interaction strength, and PEG was added to stimulate LLPS. Effectively stabilized (coalescence-free for 60 min) condensates were indicated with yellow boxes. **c,** Confocal images of cage-treated (one-pot) LAF condensates. Cage-condensate assemblies that have undergone additional optimization (a yellow arrow) are marked with a yellow box **d,** Confocal images of LAF condensates without (scaffold only) or with interfacial mi3 at increased $[Ni^{2+}]$. Effectively stabilized condensates were indicated with a yellow box. **e,** Confocal images of cage-treated (one-pot) PS2H condensates. Surface-stabilized (coalescence-free) protein condensate images are indicated with a yellow box. **f,** Confocal images of mi3-treated PS2H condensates at different salt concentrations. All scale bars, 5 μm.

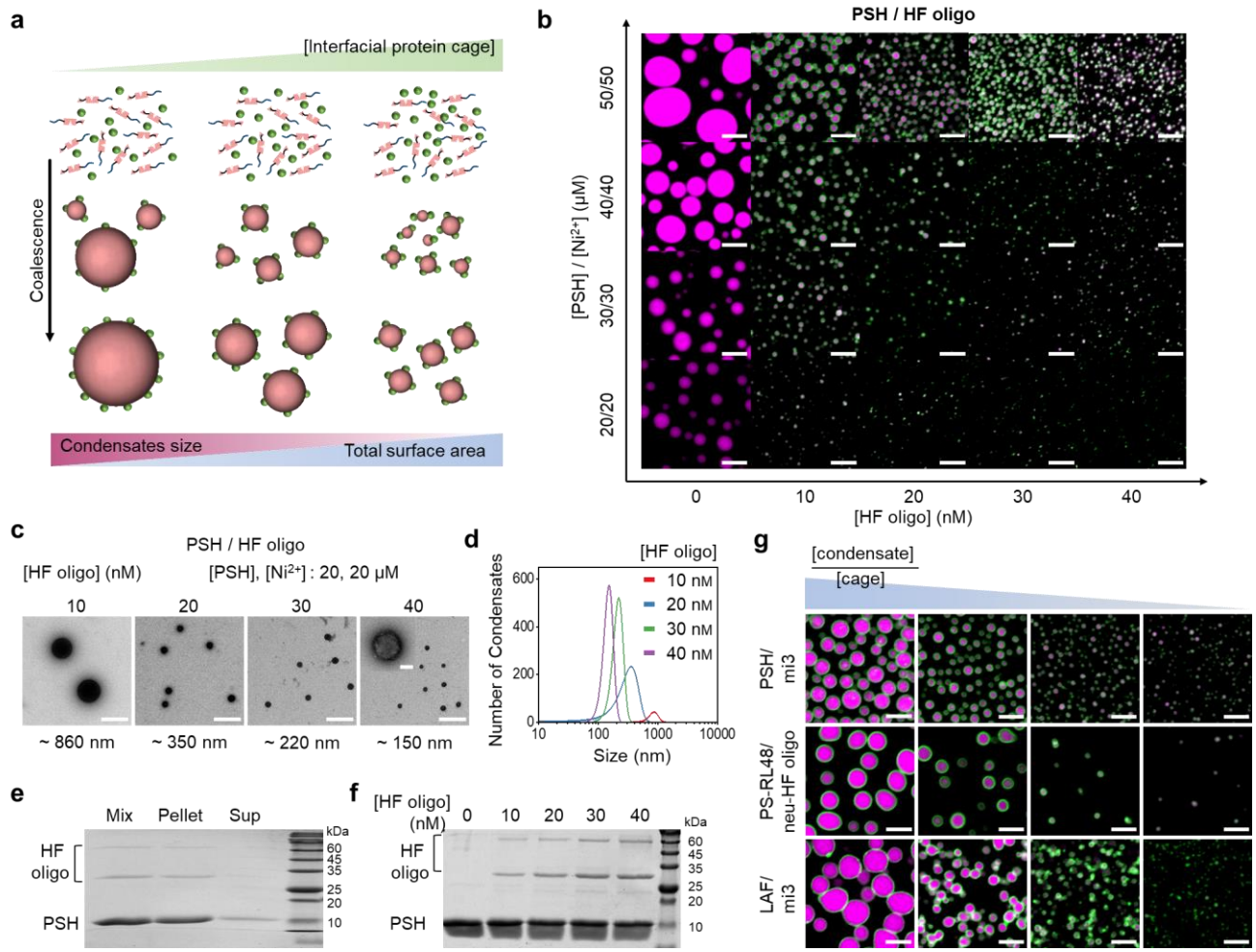

Fig. 3 | Size-controlled synthesis of cage-stabilized protein condensates. a, Schematic illustration of condensate size variation by [condensate]/[interfacial protein cages] ratios. **b,** The size diagram of HF oligo-stabilized PSH condensates with varying [PSH]/[Ni^{2+}] and [HF oligo]. Confocal images were taken after 1 h incubation upon LLPS. **c,** Negative-stained TEM images of nano-sized HF oligo-PSH condensates. Average condensate sizes are indicated below. **d,** Size distribution profiles (based on negative-stained TEM images as shown in Fig. 2c) of nano-sized HF oligo-PSH condensates. **e,** A denatured gel image of total LLPS (HF oligo-PSH) mixtures (Mix), centrifuged condensates (Pellet), and remaining substances in the dilute phase (Sup). **f,** A denatured gel image of centrifuged condensates (Pellet) synthesized with fixed [PSH] and increasing [HF oligo]. **g,** Confocal images of various cage-stabilized condensates with varying sizes by altering [condensate]/[cage]. Scale bars, **b,g,** 5 μm. **c,** 1 μm (100 nm for the enlarged image).

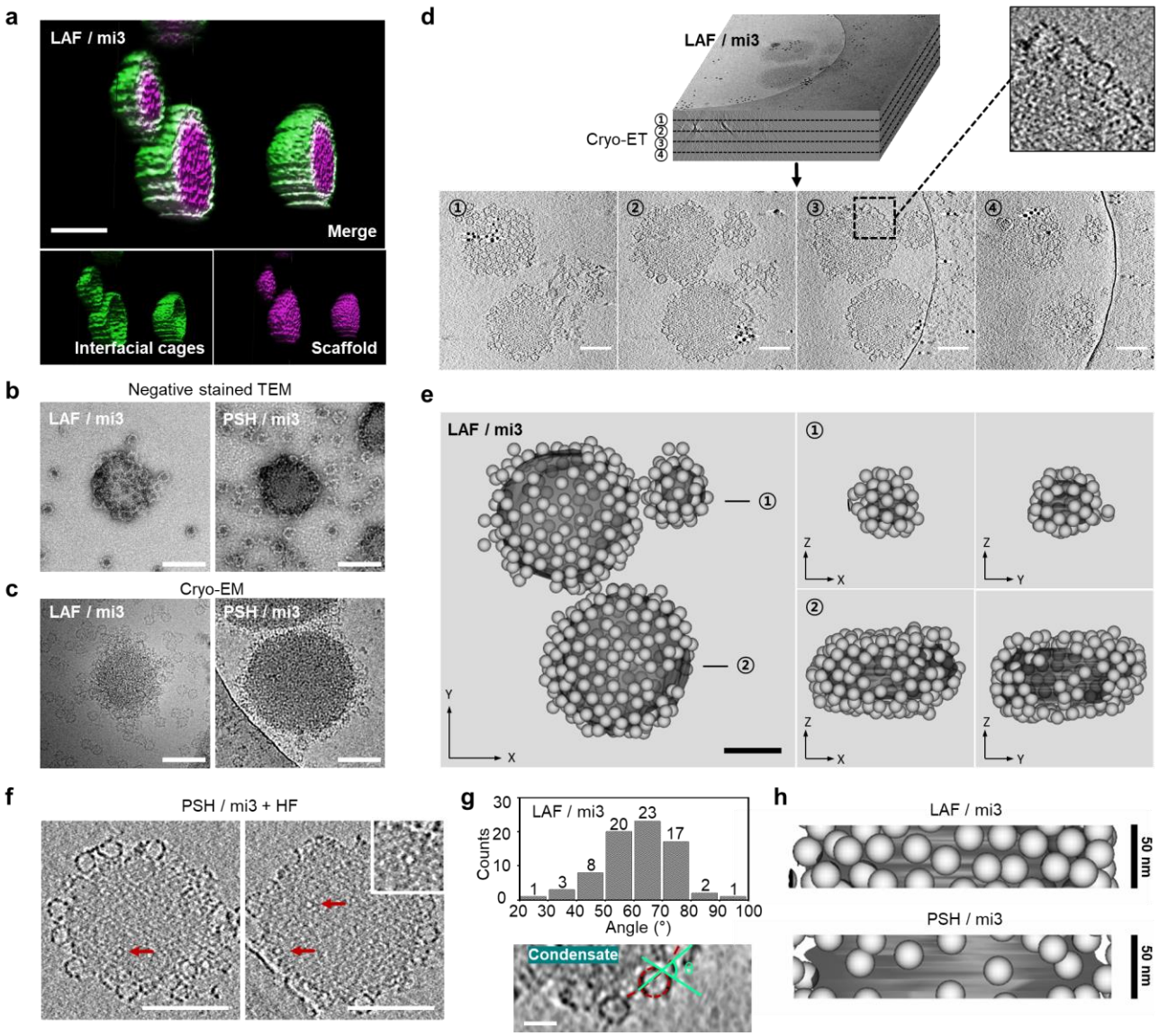

Fig. 4 | Structures of surface-stabilized protein condensates with interfacial protein cages. a, Confocal Z-stack 3D representation of mi3-LAF condensates (LAF: magenta, mi3: green). **b,** Negative-stained TEM images of mi3-LAF (left) and mi3-PSH (right) condensates. **c,** Cryo-EM images of mi3-LAF (left) and mi3-PSH (right) condensates. **d,** Reconstructed tomograms of mi3-LAF condensates. Four images of equal Z-distances (~40 nm) are shown below to demonstrate cage distributions at the bottom/middle/top of the condensate. Thick black dots are 10 nm gold nanoparticles used as a fiducial marker. **e,** 3D volume models of mi3-LAF condensates (left: top view of the whole tomogram, right: front and side view of selected condensates). mi3 cages are shown as gray spheres. **f,** Tomogram slices of mi3-PSH condensate with ferritin cages (red arrows) located inside the condensate. **g,** Contact angles of mi3 cages on LAF condensates with a representative tomogram slice image. An exemplary cage and contact condensate surface are indicated with red dotted circle and line, respectively. **h,** Side views of 3D volume models of mi3-stabilized LAF (top) and PSH (bottom) condensates. Scale bars **a,** 5 μm. **b,c,d,e,f** 100 nm **g,** 25 nm.

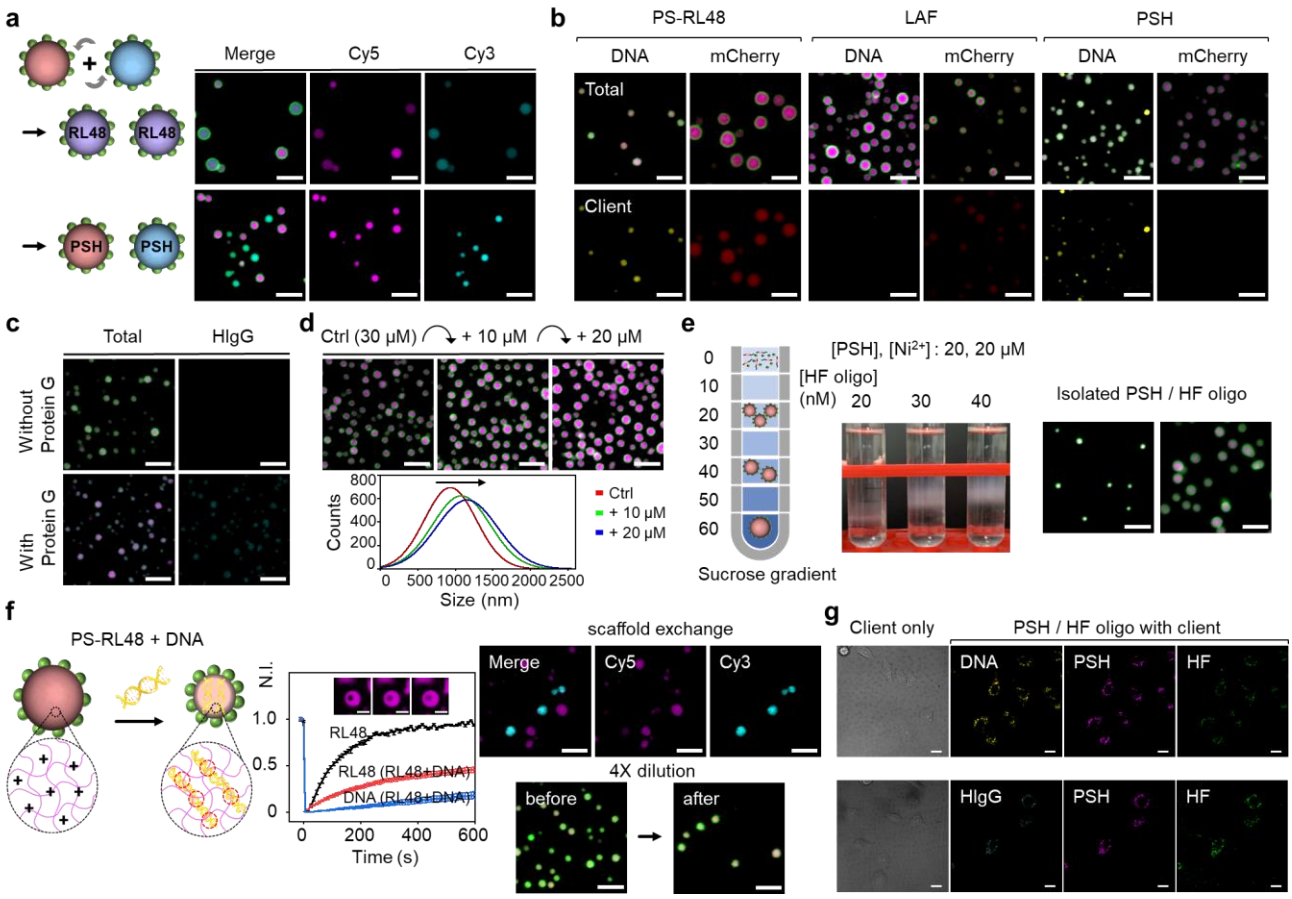

Fig. 5 | Dynamic behaviors of cage-stabilized protein condensates. a, Confocal images of separately labeled (Cy5 magenta, Cy3 cyan) cage-stabilized condensate mixtures after 10 min incubation upon mixing (top: PS-RL48 condensates, bottom: PSH condensates). **b,** Confocal images of cage-stabilized condensates with externally added client biomolecules (DNA (yellow) and mCherry-6His (red)). **c,** Confocal images of HF oligo-PSH condensates (with or without protein G fusion to PSH) synthesized with antibody (cyan). **d,** Confocal images and size distribution profiles of mi3-PSH condensates with subsequent PSH addition. Condensates were formed with 30 μM PSH, and 10 μM PSH was externally added twice. **e**, Sucrose gradient centrifugation of cage-stabilized PSH condensates. A picture of sucrose gradient centrifuged HF oligo-PSH condensates with different sizes with schematics and exemplary confocal images of isolated PSH condensates in sucrose solution are shown. **f,** Fluidity change of cage-stabilized condensates. DNAs recruited into fluidic PS-RL48 condensates induce additional PS-RL48 clustering around DNAs, resulting in decreased size and fluidity of condensates (left: schematics). FRAP recovery profiles (red: PS-RL48, blue: recruited DNA) and confocal images (PS-RL48) of the bleached DNA-containing PS-RL48 condensates are shown in the middle. A FRAP profile for fluidic PS-RL48 condensates is shown as a control (black). Confocal images for separately labeled, DNA-recruited PS-RL48 condensate mixtures after 60 min incubation (right top) and 4X diluted condensates (right bottom) are shown in the right. **g,** Confocal images of HeLa cells treated with biomolecule-encapsulated HF oligo-PSH condensates. DNA (yellow), HIgG (cyan), PSH (magenta), and HF (green). Scale bars, **a-f,** 5 μm. **g,** 10 μm.